

# Tidal deformability in neutron stars from a microscopic point of view

Francesca Sammarruca\* and Prabin Thapa

*Physics Department, University of Idaho, Moscow, ID 83844-0903, U.S.A.*

(Dated: December 2, 2025)

We present results for the tidal deformability in neutron stars, the tidal Love number  $k_2$ , and the effective deformability of a binary system. The microscopic equation of state for cold  $\beta$ -stable neutron matter is based upon high-precision two-neutron forces and includes the chiral three-neutron forces required at the chosen order. We review and motivate our choices for the high-density continuation of the microscopic equation of state. We discuss our predictions and observe that they are well within multimessenger constraints. In contrast, stiff equations of state that yield radii larger than about 13 km are ruled out by GW170817 constraints.

**Keywords:** Tidal deformability; neutron matter; neutron stars; chiral effective field theory

## I. INTRODUCTION

A fully microscopic equation of state (EoS) up to central densities of the most massive stars – potentially involving non-nucleonic degrees of freedom and phase transitions – is not within reach. Nevertheless, neutron stars are powerful natural laboratories for constraining theories of the nuclear EoS [1–6] and studying matter under extreme conditions.

A mix of all fundamental forces existing in nature is present in a neutron star, which continues to motivate the large interdisciplinary interest in its properties and the intense effort to constrain those properties both observationally and experimentally, with various levels of statistical and systematic uncertainties, see e.g. Ref. [7]. When working with microscopic predictions (as opposed to phenomenological models or statistical analyses), one must be mindful of the theory’s limitations and identify the best ways to extract and interpret information from the observational or terrestrial data.

In this paper, we focus primarily on the tidal properties of neutron stars, which reflect directly on the emitted gravitational wave signal, offering the opportunity of detecting the latter to constrain the former [8–10]. This prospect was first realized in August of 2017, with the detection of gravitational waves generated by a coalescing neutron star binary. This groundbreaking event was made possible by the second-generation ground-based detectors LIGO [11] and Virgo [12], an event known as GW170817 [1]. We can expect future observations to detect the inspiral and coalescence of more compact binary systems.

During a neutron star merger event, the gravitational field of one neutron star on the other induces tidal deformations, which are encoded in the late-inspiral gravitational wave signal. More precisely, when a neutron star is placed in the perturbing tidal gravitational field generated by its companion compact star, its shape will be distorted, resulting in an induced quadrupole moment. The induced quadrupole moment of the neutron star will impact the energy of the system and increase the rate of emission of gravitational waves, with the result that the binary system emits more energy and evolves faster towards the collision and merger [13, 14].

Compact binaries that are detectable through gravitational waves are natural systems to observe this type of interaction, which opens the way to finding additional constraints to the neutron star EoS. A stiffer EoS, where the pressure increases rapidly with density, yields stars with larger radii and larger tidal effects. Therefore, tidal distortion reflects the stiffness of the EoSs, with the inspiral proceeding more rapidly for stars with larger tidal deformability.

As we review below, for a given neutron star mass, the tidal deformability is strongly correlated with the star radius and, thus, the star compactness,  $M/R$ . Keeping in mind that accurate and precise neutron star radius measurements are challenging [15], the importance of tight constraints on global neutron star properties that depend on  $M/R$  is self-evident. We also recall that the radius of the canonical neutron star correlates with the (model dependent) slope of the symmetry energy around saturation density.

This paper is organized as follows. In Sec. II, we review briefly our theoretical ingredients, omitting details that have been published elsewhere. In Sec. III, we construct high-density continuations of the microscopic EoS, paying particular attention to the speed of sound in stellar matter. In Sec. IV A, we outline the calculation of the tidal deformability, which can be incorporated in the solution scheme used for the well-known Tolman-Oppenheimer-Volkoff (TOV) differential equations for  $\frac{dP}{dr}$  and  $\frac{dm}{dr}$ . Our results, along with other predictions and constraints, are discussed in Sec. IV B. Our main takeaways are summarized in Sec. V.

---

\* Corresponding author. Email: fsammarr@uidaho.edu

## II. BASIC CONCEPTS IN CHIRAL EFFECTIVE FIELD THEORY

The microscopic part of our equation of state for cold  $\beta$ -equilibrated neutron matter is based upon high-precision two-neutron potentials [16] and includes the chiral three-neutron forces that appear at the specified order. For a comprehensive review of nuclear forces based on chiral effective field theory (EFT), see Ref. [17].

Given an energy scale and degrees of freedom appropriate at that scale, an EFT comprises all interactions consistent with the symmetries that govern those degrees of freedom. For the nuclear problem, relevant degrees of freedom are pions (Goldstone bosons), nucleons, and  $\Delta(1232)$  isobars. We use the delta-less chiral EFT. To begin with, one writes the most general Lagrangians describing all interactions between pions, nucleons, and pions with nucleons. Because pion interactions must vanish at zero momentum transfer and in the chiral limit, where the pion mass,  $m_\pi$ , goes to zero, the corresponding Lagrangian is expanded in powers of spatial derivatives or pion masses. From these Lagrangians, an infinite number of Feynman diagrams can be generated, which seems to render the theory unmanageable. The strategy is then to design a scheme for ordering the diagrams according to their importance – the essence of Chiral Perturbation Theory (ChPT). Nuclear potentials are defined by the irreducible types among these graphs. These graphs are then analyzed in terms of powers of  $Q$ , with  $Q = p/\Lambda_b$ , where  $p$  is generic for a momentum, (nucleon three-momentum or pion four-momentum), or the pion mass, and  $\Lambda_b \sim m_\rho \sim 0.7$  GeV (with  $m_\rho$  the mass of the  $\rho$  meson) is the breakdown scale [18]. Determining the power ( $\nu$ ) has become known as power counting.

While the predictions at  $N^2$ LO are fully *ab initio*, a warning is in place for current  $N^3$ LO calculations. As pointed out in Ref. [19], there is a problem with the regularized 3NF at  $N^3$ LO (and higher orders) in all present nuclear structure calculations. The  $N^3$ LO 3NFs currently in use are regularized by a multiplicative regulator applied to the 3NF expressions as derived from dimensional regularization. This approach leads to violation of chiral symmetry at  $N^3$ LO and destroys the consistency between two- and three-nucleon forces [19, 20]. Consequently, none of the current calculations that include 3NFs at  $N^3$ LO (and beyond) can be considered truly *ab initio*. An appropriate symmetry-preserving regulator [19] should be applied to the 3NF at  $N^3$ LO from Refs. [21, 22]. At the present time, reliable predictions exist only at  $N^2$ LO, NLO, and LO. However, for the few fully *ab initio* calculations, the precision at  $N^2$ LO is unsatisfactory. A first step towards deriving consistently regularized nuclear interactions in chiral EFT has been proposed in Refs. [23, 24]. It requires the cutoff to be introduced already at the level of the effective Lagrangian. A path integral approach [23] can then be applied to the regularized chiral Lagrangian to derive nuclear forces through the standard power counting of chiral EFT.

Throughout the paper, we will show results at the (fully consistent) third order ( $N^2$ LO), and at the highest order which we have considered (fourth order, or  $N^3$ LO). For details on how our EoS are built, the reader is referred to Refs. [25, 26].

## III. THE SPEED OF SOUND IN NEUTRON STAR MATTER

### A. Subluminar and non-conformal

The content of this section is based on Ref. [27], where we discussed how causality and maximum-mass constraints pose considerable restrictions on the general features of the high-density EoS, if such continuation follows an *ab initio* portion.

Parametrizations of the high-density EoS in terms of the speed of sound can be used as an alternative to, or in combination with the popular polytropic extensions. Defining  $\rho_0$ ,  $\epsilon_0$ , and  $P_0$  as the baryon density, the energy density, and the pressure at threshold (the density at which the EoS parametrization is attached to the previous piece), we write [28, 29], for  $i \geq 1$ ,

$$\rho_i = \rho_{i-1} + \Delta\rho, \quad (1)$$

$$\epsilon_i = \epsilon_{i-1} + \Delta\epsilon, \quad (2)$$

and

$$\Delta\epsilon = \Delta\rho \frac{\epsilon_{i-1} + P_{i-1}}{\rho_{i-1}}. \quad (3)$$

A reasonable parametrization for the speed of sound is:

$$\left(\frac{v_s}{c}\right)_i^2 = 1 - c_1 \exp\left[-\frac{(\rho_i - c_2)^2}{w^2}\right], \quad (4)$$

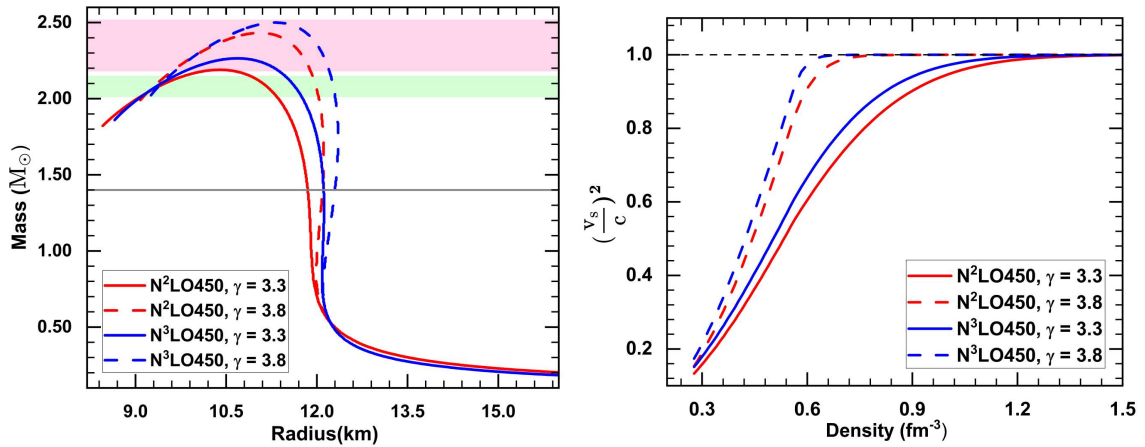


FIG. 1: Left:  $M(R)$  curves at fourth order ( $N^3\text{LO}$ , blue) and at third order ( $N^2\text{LO}$ , red) of ChPT. Dashed curves: the first extension is done using a polytrope with  $\gamma = 3.3$ , followed by pressure values given by Eq. (5) together with Eq. (4); Solid curves: obtained with  $\gamma = 3.8$ , a value beyond which the EoS begins to violate causality. Right: Dimensionless speed of sound squared corresponding to the curves on the left. Same color and pattern conventions. The figure is taken from Ref. [27].

TABLE I: Some neutron star properties corresponding to the red and the blue  $M(R)$  relations shown in Fig. 1. The Table is taken from Ref. [27].

$\gamma$	chiral order	$M_{max}/M_\odot$	$R_{M_{max}}(\text{km})$	$\rho_c(\text{fm}^{-3})$	$R_{1.4}(\text{km})$
3.3	$N^2\text{LO}$	2.19	10.39	1.09	11.84
	$N^3\text{LO}$	2.27	10.68	1.03	12.11
3.8	$N^2\text{LO}$	2.43	11.06	0.93	12.09
	$N^3\text{LO}$	2.50	11.32	0.88	12.30

where the constants  $c_1$  and  $c_2$  are determined from continuity of the speed of sound and its derivative at the threshold density.

Using the relation between the dimensionless speed of sound squared and  $dP/d\epsilon$ , we write the pressure above the threshold as

$$P_i = \left(\frac{v_s}{c}\right)_{i-1}^2 \Delta\epsilon + P_{i-1}, \quad (5)$$

where we have This EoS continuation is obviously causal at all densities and allows for a maximum mass of  $2.07 M_\odot$ .

We found [27] that a better ansatz, for the purpose of achieving high maximum masses while respecting causality at any density, is to first continue the EoS with a relatively steep polytrope,

$$P(\rho) = \alpha(\rho)^\gamma, \quad (6)$$

and then follow with a parametrization as in Eqs. (4–5), which will remain causal by construction. The matching densities are  $0.277 \text{ fm}^{-3}$  and  $0.563 \text{ fm}^{-3}$  [27]. The resulting  $M(R)$  curves are shown on the LHS of Fig. 1 for both  $N^3\text{LO}$  (blue) and  $N^2\text{LO}$  (red). For the dashed curves, the first extension is a polytrope with  $\gamma = 3.3$ , followed by pressure values obtained from Eq. (5) with the speed of sound (SoS) given in Eq. (4). The solid curves (same color convention) have been obtained with  $\gamma = 3.8$ , a value beyond which the EoS begins to violate causality. On the RHS, we show the dimensionless speed of sound squared corresponding to the curves on the left. Table I displays the maximum mass, its radius, the central density, and the radius of the canonical mass neutron star, for the curves in Fig. 1. It is important to recall that the radius of a  $1.4 M_\odot$  is sensitive to the pressure at normal nuclear densities and thus it can pose constraints on ab initio theories of the EoS at those densities where the theories can be applied reliably.

In Ref. [27], we concluded that a polytrope connecting the chiral EFT predictions with a causality-maintaining parametrization has a limited range of powers. We underlined that this scenario is fundamentally related to the softness of the chiral predictions. Therefore, the nature of the predictions at normal density have a far-reaching impact, which extends to densities up to a few times normal density.

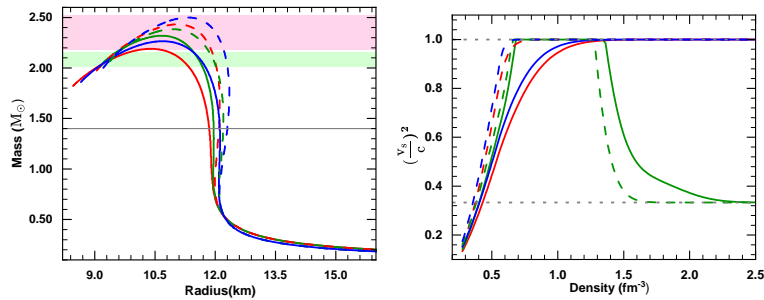


FIG. 2: Left: the red and blue  $M(R)$  curves are as described in Fig. 1. Green curves:  $M(R)$  relations at  $N^3LO$  (dashed) and at  $N^2LO$  (solid) where the polytropic part of the EoS has adiabatic index equal to 3.5, and the last continuation is based on the conformal speed of sound parametrization, Eq. (7). Right: Dimensionless speed of sound squared corresponding to each of the cases displayed on the left. See text for additional explanation.

### B. Subluminar and conformal

In the QCD limit of deconfined quarks in the presence of asymptotic freedom, quarks should behave like free fermions. Some perturbative QCD calculations [30] support the conformal limit,  $(v_s/c)^2 = 1/3$ . We observed that an EoS that's subconformal at all densities (that is, Eq. (4) with the asymptotic limit replaced by 1/3), cannot generate sufficiently large masses. On the other hand, the speed of sound can be asymptotically conformal and non-monotone. A scenario where the speed of sound peaks around few to several times nuclear density and then falls back to approach the QCD limit for deconfined quark matter would signify some sort of phase transition with the conformal limit reached well beyond central densities of the heaviest observed neutron stars. The superconformality condition,  $\left(\frac{v_s}{c}\right)^2 > 1/3$ , satisfied *on the average* in neutron stars may have fundamental implications on the trace of the energy-momentum tensor at the center of rotating neutron stars [31].

Here, we will explore parametrizations where the speed of sound is consistent with the conformal limit as the density approaches infinity. This can be simulated adding a second, skewed gaussian function to Eq. (4), and of course changing the asymptotic value to 1/3:

$$\left(\frac{v_s}{c}\right)_i^2 = \frac{1}{3} - c_1 \exp\left[-\frac{(\rho_i - c_2)^2}{w^2}\right] + c_3 \exp\left[-\frac{(\rho_i - c_4)^2}{w_2^2}\right] \left[1 + \text{erf}\left(c_5 \frac{(\rho_i - c_4)}{w_2}\right)\right]. \quad (7)$$

We solve for  $c_1$  and  $c_2$  as done above, matching Eq. (7) and its derivative to the values at threshold, within a chosen parameter space for the remaining three coefficients,  $c_3, c_4, c_5$ . The widths  $w$  and  $w_2$  are obtained by normalizing both gaussians in the standard way. Although this procedure can provide a very large number of possibilities, we observed that the roots,  $c_1$  and  $c_2$ , converge easily within limited ranges for the free parameters:  $c_3 \approx [0, 1]$ ,  $c_4 \approx [1, 4] \text{ fm}^{-3}$ ,  $c_5 \approx [-50, 50]$ . In fact, the roots tend to cluster around a few pairs of  $c_1, c_2$  values, weakly sensitive to the large variations in  $c_5$ , and only moderately sensitive to variations of  $c_3$  and  $c_4$ . As a consequence, those parametrizations produce very similar  $M(R)$  results. A representative case is shown by the green curves on the left-hand side of Fig. 2, where we have chosen a polytropic index of 3.5 to ensure that the new curves would stand out in between the other two sets from Fig. 1. The corresponding curves for the dimensionless speed of sound are seen to approach the conformal limit on the right-hand side of Fig. 2. We also note that implementing the conformal limit at all densities would not allow sufficiently large masses. Maximum masses as large as those recently observed require a rapid rise of the pressure soon after the first matching point.

It is interesting to observe that the left panels in Fig. 1 and Fig. 2 are consistent with each other, in the sense that the green curves are what one would expect from the non-conformal calculation and an adiabatic index that's in between the other two. In contrast, the green predictions on the right are dramatically different from the red or blue predictions. This suggests that the maximum mass is only weakly sensitive to the super-high density behavior of the EoS.

## IV. TIDAL DEFORMABILITY

### A. General aspects

The tidal deformability is a parameter that quantifies how easily the star is deformed by an external tidal field. Therefore, a large tidal deformability signals a larger and less compact star which deforms easily.

A spherically symmetric star placed in a quadrupolar tidal field  $\epsilon_{ij}$ , the response to the perturbation is a quadrupole moment,  $Q_{ij}$ , which, to linear order in  $\epsilon_{ij}$ , can be written as

$$Q_{ij} = -\lambda_t \epsilon_{ij} . \quad (8)$$

In the Newtonian limit, the perturbing tidal field,  $\epsilon_{ij}$ , is the second spacial derivative of the external field, resulting in units of inverse length squared [59]. The quadrupole moment has units of length cubed. We expect  $\lambda_t$  to be proportional to the fifth power of the neutron star radius,  $R$ . Adopting traditional convention, we express the tidal deformability as

$$\lambda_t = \frac{2}{3} k_2 R^5 , \quad (9)$$

where  $k_2$  is the gravitational Love number. Of greater astrophysical relevance is the dimensionless tidal deformability, defined as

$$\Lambda = \frac{\lambda_t}{M^5} = \frac{2}{3} k_2 C^{-5} , \quad (10)$$

where  $C$  is the previously defined neutron star's compactness. It is  $\Lambda$  that actually governs the effects of tides on inspiral waveforms [32].

Given a proposed equation of state, the tidal deformability of a neutron star of a certain mass can be obtained by computing the metric in the asymptotic regime using the Einstein equations, extracting the corresponding  $r$ -order terms, and taking their ratio. The ensuing calculation is described in detail in Ref. [14]. The result is an expression for the gravitational Love number,  $k_2 = k_2(C, y_R)$ , with  $y_R$  the solution at the star's surface of the first order differential equation

$$y'(r) + (1/r)y^2(r) + (1/r)y(r)e^{\lambda(r)} 1 + 4\pi r^2 [p(r) - \epsilon(r)] + rQ(r) = 0 , \quad (11)$$

In the equation above, the metric function for a spherical star is

$$e^{\lambda(r)} = [1 - 2m(r)/r]^{-1} , \quad (12)$$

and

$$Q(r) = 4\pi e^{\lambda(r)} [5\epsilon(r) + 9p(r) + (\epsilon(r) + p(r))/c_s^2(r) - 6e^{2\lambda(r)}/r^2 - 4e^{\lambda(r)}/r^4 [m(r) + 4\pi p(r)r^3]^2] , \quad (13)$$

where  $m(r)$ ,  $\epsilon(r)$ , and  $p(r)$  are the enclosed mass, the energy density, and the pressure at a radial distance  $r$ .

The Love number,  $k_2$ , is obtained in terms of  $C$  and the value of  $y(r)$  at  $r = R$ ,  $y_R$ , from

$$\begin{aligned} k_2(C, y_R) = & \frac{8}{5} C^5 (1 - 2C)^2 [2 - y_R + 2C(y_R - 1)] \{2C[6 - 3y_R + 3C(5y_R - 8)] + \\ & 4C^3[13 - 11y_R + C(3y_R - 2) + 2C^2(1 + y_R)] + \\ & 3(1 - 2C)^2[2 - y_R + 2C(y_R - 1)] \ln(1 - 2C)\}^{-1} , \end{aligned} \quad (14)$$

and then used in Eq.( 10) to determine the tidal deformability.

### B. Results and discussion

#### 1. Tidal deformability and tidal Love number

On the left side of Fig. 3, we show the dimensionless tidal deformability for the four cases considered in Fig. 1. For comparison, the pink dots are taken from the Bayesian analysis of Ref. [33] and represent the most probable

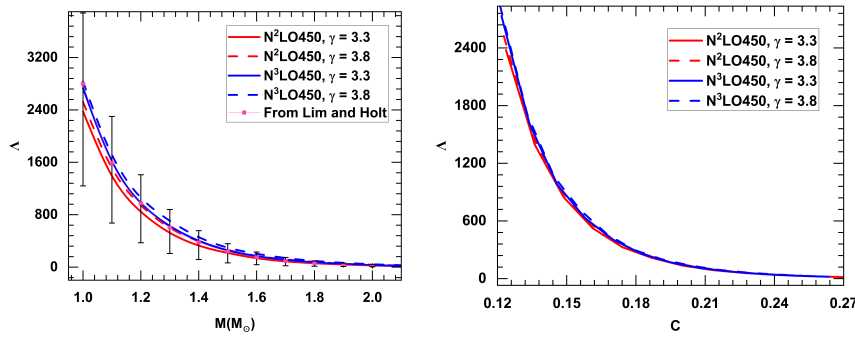


FIG. 3: Left: The dimensionless tidal deformability as a function of the neutron star mass (left) and as a function of the compactness (right). The pink dots and their uncertainties are taken from the Bayesian analysis of Ref. [33]. See text for more details.

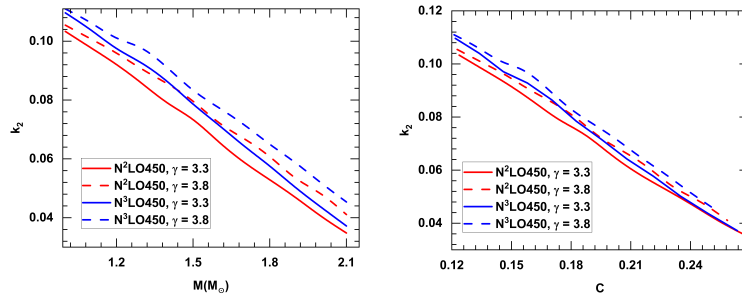


FIG. 4: Left: The tidal Love number as a function of the neutron star mass (left) and as a function of the compactness (right).

values from sampling 300,000 EoS models based on chiral EFT and experimental constraints. The vertical bars show the uncertainties at the  $2\sigma$  level. All of our predictions are close to each other and quite consistent with the most probable outcomes from the Bayesian analysis. On the right of the figure, our predictions are displayed *versus* the star's compactness.

Closely related to  $\Lambda$  is the tidal Love number  $k_2$ , related to  $\Lambda$  as in Eq. (10). This is shown in Fig. 4 as a function of the neutron star mass and compactness. Often, comparison between relativistic and Newtonian calculations or tabulations of deformation properties for polytropic EoS with different polytropic indices are given in terms of  $k_2$  rather than  $\Lambda$  [14]. Our predicted values of  $k_2$  are shown in Table II for a representative case.

TABLE II: Compactness and tidal Love number as a function of the neutron star mass for one of the EoS used in Fig. 4.

EoS	$M/M_\odot$	C	$k_2$
$N^2LO \gamma=3.3$	0.90	0.112	0.105
	1.0	0.125	0.103
	1.1	0.137	0.0972
	1.2	0.150	0.0926
	1.3	0.163	0.0853
	1.4	0.175	0.0782
	1.5	0.188	0.0722
	1.6	0.202	0.0660
	1.7	0.215	0.0579
	1.8	0.230	0.0521
	1.9	0.245	0.0428
	2.0	0.261	0.0361
	2.2	0.313	0.0161

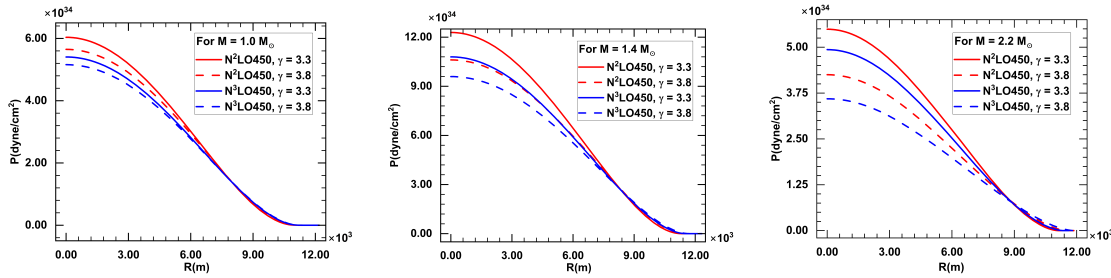


FIG. 5: Pressure profile in neutron stars with different masses as given in the inset.

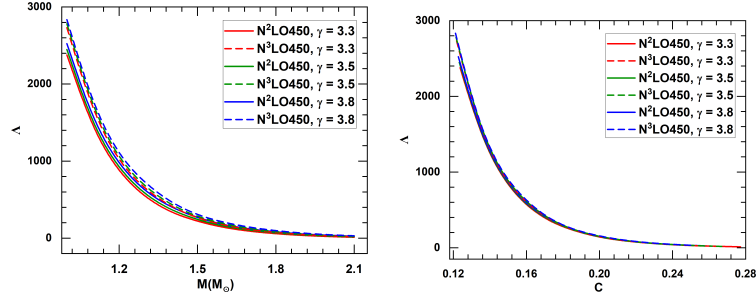


FIG. 6: Tidal deformability as a function of mass (left) and compactness (right). The green curves are based on the EoS extended to the highest densities with a conformal parametrization of the speed of sound.

In the context of compactness and tidal deformability, it is insightful to look at the pressure profile of neutron stars with different masses, see Fig. 5. As expected, the central pressure is largest (smallest) for the EoS that results in the smallest (largest) radius for the same mass, compare with Fig. 1.

Recent multimeshanger constraints can be found in Ref. [34], obtained from various methodologies based on variants of the GW170817 data sets. Their most robust constraint is based on a combination of GW-based findings and EoS-independent X-ray constraints, and is reported as

$$\Lambda_{1.4} = 265.18^{+237.88}_{-104.38} \quad R_{1.4} = 11.53^{+0.89}_{-0.88} \text{ km} , \quad (15)$$

for the dimensionless tidal deformability and radius of the canonical mass neutron star. We underline that this EoS-independent constraint is yet another confirmation that the large radius extracted from the PREX neutron skin measurement [35] is unrealistic.

Accounting for both chiral truncation error and the spreading due to different values of  $\gamma$ , we estimate our ranges for  $\Lambda_{1.4}$  and  $R_{1.4}$  at N<sup>2</sup>LO to be

$$\Lambda_{1.4} = 355.25 \pm 85.64 \quad R_{1.4} = (11.99 \pm 0.51) \text{ km} , \quad (16)$$

quite consistent with Eq. (15). We underline that the overall uncertainties in Eq. (16) are evaluated at N<sup>2</sup>LO, which, at this time, is a fully consistent order, see comments in Sec. II.

Other inferred upper limits on neutron star radii and tidal deformabilities from GW170817 rule out stiff equations of state that result in large radii and large tidal deformabilities. Recent estimates of the measurability of tidal effects and the ability of these observatories to constrain the EoS with signals from black hole-neutron star and binary neutron star systems can be found in Refs. [36–40] and references therein.

Next, we want to explore the sensitivity of  $\Lambda$  to the high-density parametrization of the speed of sound discussed in Sec. IIIB. For that purpose, we employ the four EoS used for Fig. 2, keeping the same color and pattern conventions. As for the M(R) results on the left side of Fig. 2, we see that the green curves are what we would expect from the non-conformal calculation and an adiabatic index that's between the other two, while the speed of sound predictions with or without the conformal limit are dramatically different, see right side of Fig. 2. This seems to indicate that the tidal deformability is mostly sensitive to the EoS at medium to moderately high densities, a regime that “feels” the influence of the microscopic theory [27], as discussed in Sec. IIIA.

TABLE III: Effective tidal deformability under the GW170817 conditions.

$q = M_2/M_1$	$M_1/M_\odot$	$M_2/M_\odot$	$\tilde{\Lambda}$
0.73	(1.599, 1.600)	(1.167, 1.168)	(390.32, 388.61)
0.75	(1.577, 1.584)	(1.183, 1.188)	(393.76, 384.96)
0.80	(1.526, 1.532)	(1.221, 1.226)	(399.19, 389.61[)
0.85	(1.479, 1.486)	(1.257, 1.263)	(401.30, 380.37)
0.90	(1.437, 1.443)	(1.293, 1.299)	(392.83, 382.89)
0.95	(1.398, 1.404)	(1.328, 1.334)	(396.11, 383.23)
1.0	(1.363, 1.369)	(1.363, 1.369)	(393.71, 383.98)

## 2. The mass-weighted tidal deformability

Here, we focus on our results for the effective tidal deformability,  $\tilde{\Lambda}$ , for a binary with masses (deformabilities)  $M_1(\Lambda_1)$  and  $M_2(\Lambda_2)$ . First, we recall that  $\Lambda_1$  or  $\Lambda_2$  cannot be disentangled in the observed gravitational wave, and thus are not directly observable. Instead, it is possible to constrain the mass-weighted average (or effective) tidal deformability,

$$\tilde{\Lambda} = \frac{16}{13} \frac{(M_1 + 12M_2)M_1^4\Lambda_1 + (M_2 + 12M_1)M_2^4\Lambda_2}{(M_1 + M_2)^5} , \quad (17)$$

with  $M_1$  and  $M_2$  the masses of the primary and the secondary neutron stars in the binary.  $\tilde{\Lambda}$  determines the total effect of the tidal deformability on the phase evolution of the GW signal. Another observable that can be extracted from the evolution of the frequency in the observed GW signal is the chirp mass, defined as

$$M_c = \frac{(M_1 M_2)^{3/5}}{(M_1 + M_2)^{1/5}} = M_1 \frac{q^{3/5}}{(1+q)^{1/5}} , \quad (18)$$

with  $q = M_1/M_2$ . The chirp mass is one of the most tightly constrained properties extracted from GW170817. Therefore,  $M_c$  can be set equal to the observed value for the purpose of comparing predictions of  $\tilde{\Lambda}$  with experimental data. The GW170817 constraint was stated as  $M_c/M_\odot = 1.188^{+0.004}_{-0.002}$  at the 90% confidence level [1], from which the primary and secondary masses (in units of  $M_\odot$ ), were inferred to be within the range (1.36, 1.60) and (1.17, 1.36), respectively, placing  $q$  between 0.73 and 1. We exploited this information to calculate the values in Table III. Starting with  $M_1$  in the full range of masses inferred from GW170817, (1.17, 1.60), and imposing the very stringent  $M_c$  constraint, we obtain  $\tilde{\Lambda}$  for each value of  $q$ , see Table III. The effective tidal deformability changes by about 4% across the  $q$ -variations. Essentially,  $\tilde{\Lambda}$  is constrained at fixed mass.

As we already pointed out when discussing  $\Lambda_{1.4}$ , one of the most physically interesting aspect of the GW170817 data is the opportunity to extract constraints on the radius of the canonical mass neutron star and thus discriminate among various EoS. In Fig. 7, the shaded area represents constraints from GW170817 and AT2017gfo [41], which confine  $\tilde{\Lambda}$  to the interval (197, 720). The curve is a typical power law parametrization of  $\tilde{\Lambda}$  as a function of  $R_{1.4}$ , see Ref. [42] and references therein. Clearly, radii smaller than 10.8 km and larger than about 13 km are ruled out.

## V. CONCLUSIONS AND OUTLOOK

As noted in Ref. [27], the maximum-mass constraint moving to higher values, together with the causality requirement at any central density, poses significant restrictions on the high-density continuation of the EoS. Based on those considerations, we selected a small number of EoS differing in the chiral order and/or the adiabatic index of their polytropic portion, followed by a parametrization of the pressure vs. density that guarantees causality. We also used a parametrization where the speed of sound approaches the conformal limit at infinity and observed no significant effect.

We focused on the tidal deformability of neutron stars and related parameters, such as the tidal Love number. Our predictions are consistent with multimessenger constraints, as well as terrestrial laboratory constraints.

We addressed the effective tidal deformability of the binary and the implication of a very tight constraint on the chirp mass of the system. Measurement of the effective tidal deformability (at nearly fixed mass) can be used to extract constraints on the neutron star radius. This is very valuable, as precise neutron star radii would discriminate between equations of state better than any other single measurement. The upper limit on the effective tidal deformability from

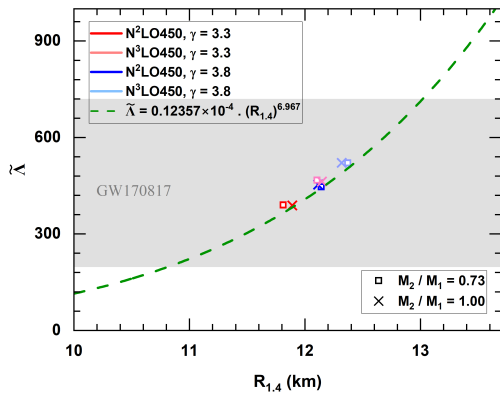


FIG. 7: Effective deformability vs. the radius of the canonical mass neutron star. The shaded area represents constraints from GW170817 and AT2017gfo [41]. The continuous curve is a parametrization of  $\tilde{\Lambda}$  vs.  $R_{1.4}$  [42]. Our predictions are indicated by the squares ( $q=0.73$ ) and the crosses ( $q=1.0$ ).

GW170817 excludes radii larger than 13.2 km, essentially independent of the assumed masses for the component stars. This rules out the findings from PREX II and any steep EoS that generates large radii. We underline the importance of EoS-independent measurements, which can help interpret divergent outcomes from terrestrial experiments that rely on EoS modeling assumptions.

One of our main takeaways is that, while phenomenological extensions of the EoS are unavoidable, they can and must be controlled. Extensions of the (soft) chiral EFT EoS are generally consistent with both terrestrial and observational constraints. With the new generation of GW detectors and continuing progress toward ab initio nuclear theory, there is real hope to build a robust bridge connecting microscopic physics and telescope physics.

### Acknowledgments

This work was supported by the U.S. Department of Energy, Office of Science, Office of Basic Energy Sciences, under Award Number DE-FG02-03ER41270.

### In Memoriam

*F.S. dedicates this work to Rup, with everlasting love.*

---

[1] B. P. Abbott, et al., GW170817: Observation of Gravitational Waves from a Binary Neutron Star Inspiral, *Phys. Rev. Lett.* 119 (16) (2017) 161101.

[2] Abbott, B. P. and *et al.*, Multi-messenger Observations of a Binary Neutron Star Merger, *Astrophys. J. Lett.* 848 (2) (2017) L12.

[3] Abbott, B. P. and *et al.*, GW170817: Measurements of neutron star radii and equation of state, *Phys. Rev. Lett.* 121 (16) (2018) 161101.

[4] B. P. Abbott, et al., GWTC-1: A Gravitational-Wave Transient Catalog of Compact Binary Mergers Observed by LIGO and Virgo during the First and Second Observing Runs, *Phys. Rev. X* 9 (2019) 031040.

[5] M. C. Miller, et al., PSR J0030+0451 mass and radius from NICER and implications for the properties of neutron star matter, *Astrophys. J. Lett.* 887 (2019) L24.

[6] M. C. Miller, et al., The Radius of PSR J0740+6620 from NICER and XMM-Newton Data, *Astrophys. J. Lett.* 918 (2) (2021) L28.

[7] D. Soumi, D. Finstad, J. M. Lattimer, D. A. Brown, E. Berger, C. M. Biwer, Tidal deformabilities and radii of neutron stars from the observation of gw170817, *Phys. Rev. Lett.* 121 (2018) 091102.

[8] J. A. Faber, F. A. Rasio, Binary neutron star mergers, *Living Reviews in Relativity* 15 (2012) 8.

- [9] L. Baiotti, L. Rezzolla, Binary neutron-star mergers: a review of einstein's richest laboratory, *Rep. Prog. Phys.* 80 (2017) 096901.
- [10] L. Baiotti, Gravitational waves from neutron star mergers and their relation to the nuclear equation of state, *Prog. Part. Nucl. Phys.* 109 (2019) 103714.
- [11] C. Adams, et al., Advanced LIGO, *Class. Quantum Grav.* 32 (2015) 074001.
- [12] F. Acernese, et al., Advanced Virgo: a second-generation interferometric gravitational wave detector, *Class. Quantum Grav.* 32 (2015) 024001.
- [13] E. E. Flanagan, T. Hinderer, Constraining neutron star tidal love numbers with gravitational wave detectors, *Phys. Rev. D* 77 (2008) 021502.
- [14] T. Hinderer, Tidal love numbers of neutron stars, *Astrophys. J.* 677 (2008) 1216.
- [15] S. Khadkikar, et al., Precise and accurate neutron star radius measurements with next-generation gravitational wave detectors, *Phys. Rev. D* 112 (2025) 063020.
- [16] D. R. Entem, R. Machleidt, Y. Nosyk, High-quality two-nucleon potentials up to fifth order of the chiral expansion, *Phys. Rev. C* 96 (2) (2017) 024004.
- [17] R. Machleidt, F. Sammarruca, Recent advances in chiral eft based nuclear forces and their applications, *Journal of Progress in Particle and Nuclear Physics* 137 (2024) 104117.
- [18] R. J. Furnstahl, N. Klco, D. R. Phillips, S. Wesolowski, Quantifying truncation errors in effective field theory, *Phys. Rev. C* 92 (2) (2015) 024005.
- [19] E. Epelbaum, H. Krebs, P. Reinert, High-precision nuclear forces from chiral EFT: State-of-the-art, challenges and outlook, *Front. in Phys.* 8 (2020) 98.
- [20] E. Epelbaum, H. Krebs, P. Reinert, Semi-local nuclear forces from chiral EFT: state-of-the-art and challenges, in: Tanihata, I., Toki, H., Kajino, T. (eds), *Handbook of Nuclear Physics*, Springer, Singapore (2023).
- [21] V. Bernard, E. Epelbaum, H. Krebs, U.-G. Meissner, Subleading contributions to the chiral three-nucleon force. I. Long-range terms, *Phys. Rev. C* 77 (2008) 064004.
- [22] V. Bernard, E. Epelbaum, H. Krebs, U. G. Meissner, Subleading contributions to the chiral three-nucleon force II: Short-range terms and relativistic corrections, *Phys. Rev. C* 84 (2011) 054001.
- [23] H. Krebs, E. Epelbaum, Towards consistent nuclear interactions from chiral Lagrangians I: The path integral approach, *arXiv:2311.10893 [nucl-th]* (2023).
- [24] H. Krebs, E. Epelbaum, Towards consistent nuclear interactions from chiral Lagrangians II: Symmetry preserving regularization, *arXiv:2312.13932 [nucl-th]* (2023).
- [25] F. Sammarruca, R. Millerson, Analysis of the neutron matter equation of state and the symmetry energy up to fourth order of chiral effective field theory, *Phys. Rev. C* 104 (3) (2021) 034308.
- [26] F. Sammarruca, R. Millerson, The Equation of State of Neutron-Rich Matter at Fourth Order of Chiral Effective Field Theory and the Radius of a Medium-Mass Neutron Star, *Universe* 8 (2) (2022) 133.
- [27] F. Sammarruca, T. Ajagbonna, General features of the stellar matter equation of state from microscopic theory, new maximum-mass constraints, and causality, *Front. Astron. Space Sci.* 12 (2025) 1554123.
- [28] A. Kanakis-Pegios, P. S. Koliogiannis, C. C. Moustakidis, Probing the Nuclear Equation of State from the Existence of a  $\approx 2.6 M_{\odot}$  Neutron Star: The GW190814 Puzzle, *Symmetry* 13 (2021) 183.
- [29] I. Tews, J. Carlson, S. Gandolfi, S. Reddy, Constraining the speed of sound inside neutron stars with chiral effective field theory interactions and observations, *Astrophys. J.* 860 (2) (2018) 149.
- [30] L. Brandes, W. Weise, N. Kaiser, Inference of the sound speed and related properties of neutron stars, *Phys. Rev. D* 107 (2023) 014011.
- [31] R. F. P. Mendes, C. F. Sodré, F. T. Falciano, Exceeding the conformal limit inside rotating neutron stars: Implication to modified theories of gravity, *Phys. Rev. D* 110 (2024) 104027.
- [32] E. D. Van Oeveren, J. L. Friedman, Upper limit set by causality on the tidal deformability of a neutron star, *Phys. Rev. D* 95 (2017) 083014.
- [33] Y. Lim, J. W. Holt, Bayesian modeling of the nuclear equation of state for neutron star tidal deformabilities and GW170817, *Eur. Phys. J. A* 55 (11) (2019) 209. \path{arXiv:1902.05502}, \path{doi:10.1140/epja/i2019-12917-9}.
- [34] C. Huang, Model-independent determination of the tidal deformability of a  $1.4 m_{odot}$  neutron star from gravitational-wave measurements, *Astro. J.* 985 (2025) 216.
- [35] B. T. Reed, F. J. Fattoyev, C. J. Horowitz, J. Piekarewicz, Implications of PREX-2 on the Equation of State of Neutron-Rich Matter, *Phys. Rev. Lett.* 126 (17) (2021) 172503. \path{arXiv:2101.03193}, \path{doi:10.1103/PhysRevLett.126.172503}.
- [36] K. Hotokezaka, K. Kyutoku, Y.-i. Sekiguchi, M. Shibata, Measurability of the tidal deformability by gravitational waves from coalescing binary neutron stars, *Phys. Rev. D* 93 (2016) 064082.
- [37] T. Damour, A. Nagar, L. Villain, Measurability of the tidal polarizability of neutron stars in late-inspiral gravitational-wave signals, *Phys. Rev. D* 85 (2012) 123007.
- [38] W. Del Pozzo, T. Li, M. Agathos, C. Van Den Broeck, S. Vitale, Demonstrating the Feasibility of Probing the Neutron-Stars Equation of State Second-Generation Gravitational-Wave Detectors, *Phys. Rev. Lett.* 111 (2013) 071101.
- [39] M. Agathos, et al., Constraining the neutron star equation of state with gravitational wave signals from coalescing binary neutron stars, *Phys. Rev. D* 92 (2015) 023012.
- [40] L. Wade, et al., Systematic and statistical errors in a bayesian approach to the estimation of the neutron-star equation of state using advanced gravitational wave detectors, *Phys. Rev. D* 89 (2014) 103012.
- [41] M. W. Coughlin, et al., Constraints on the neutron star equation of state from at2017gfo using radiative transfer simulations,

MNRAS 480 (2018) 3871.

[42] P. S. Koliogiannis, A. Kanakis-Pegios, C. C. Moustakidis, Neutron stars and Gravitational Waves: the Key Role of Nuclear Equation of State , Foundations 1 (2021) 217.